Chapter 7

Nano network of coordination polymer AHMT-Ag for the effective and broad spectrum detection of 6-mercaptopurine in urine and blood serum Nano network

7.1 Introduction

Nanocrystalline coordination polymers (NCCPs) are an attractive class of tailorable material and exhibit outstanding properties that expands the scope in various areas [Rodpun et al., 2016]. The significant research interest in the domain of these important scaffold due to their specific size, structural regularity, high surface area, high porosity, design ability and easy tunability results to a larger potential in different applications [Pan et al., 2004; Rowsell et al., 2004; Gupta et al., 2010; Xu et al., 2015]. Nano size of these crystalline coordination polymeric regimes is of large significance in catalysis, thin film devices and drug delivery [Tiwari et al., 2016; Vinita et al., 2018]. Owing to these features, recent research affords for the sketch of fashionable organization of metal ions with organic tecton results with huge potential for various applications [Ren et al., 2010; Melvin et al., 2010; Cho et al., 2014]. Geometry and coordination manner of organic tecton and metal center affects the properties and structure of nanocrystalline coordination polymer, other secondary interactions, such as hydrogen bonding results the versatile properties of NCCPs [Tiwari et al., 2016; Jambovane et al., 2016]. In this regard, 4-amino-3-hydrazino-5mercapto-1,2,4-triazole (AHMT), an efficient organic tecton used for production of functional NCCP. Nitrogen and sulphur atoms facilitate coordination of organic tecton with metal ion throughout the arrangement to create functional structure. Due to structural tailor ability of the organic tectons and their capability to regulate the assembly with metal ion at the nano-extent, they have fascinating applications in energy storage [Lee et al., 2009], catalysis [Vinita et al., 2018], adsorption [Furukawa et al., 2007], efficient contrast agents [Rieter et al., 2006], biotechnology [Cohen et al., 2010], nanofluids [Jambovane et al., 2016], gas separation

[Bétard et al., 2012], chemical sensing [Wang et al., 2016; Jaros et al., 2018], light harvesting [Lee et al., 2011], device formation [Xu et al., 2018] and drug delivery [Imaz et al., 2010], selective catalysis [Nirala et al., 2018], fuel cells [Inukai et al., 2016] etc. The prominent interactions are metal–ligand interactions that create extra strong entities. Further, the π–π stacking between polymer chains and inter and intra hydrogen bonds direct towards an organization and definite alignment of these structures [Haedler et al., 2015].

In the view of above particulars, our research interests is the preparation of unique nano sized coordination polymers with reasonable organic building blocks and electrochemical sensing of frequently used drug, Here we first time explore development of AHMT-Ag nanocrystalline coordination polymers (NCCPs) having identical crystalline structure, high solvent dispersibility, and electrochemical activity for sensing application.

AHMT-Ag NCCP was formulated in optimal conditions at ambient temperature without any additional supplements. The reactant concentration is optimized while synthesis and monitored using appropriate characterization techniques. During synthesis the Ag (I) ions coordinates to nitrogen and sulphur atoms of linker resulting in exceptional capability requisite for molecular amendment of the inner pore architecture. Thus, NCCPs cover huge advantages for the valuable application. This platform is advantageous for various sensing application due to its multiple binding sites.

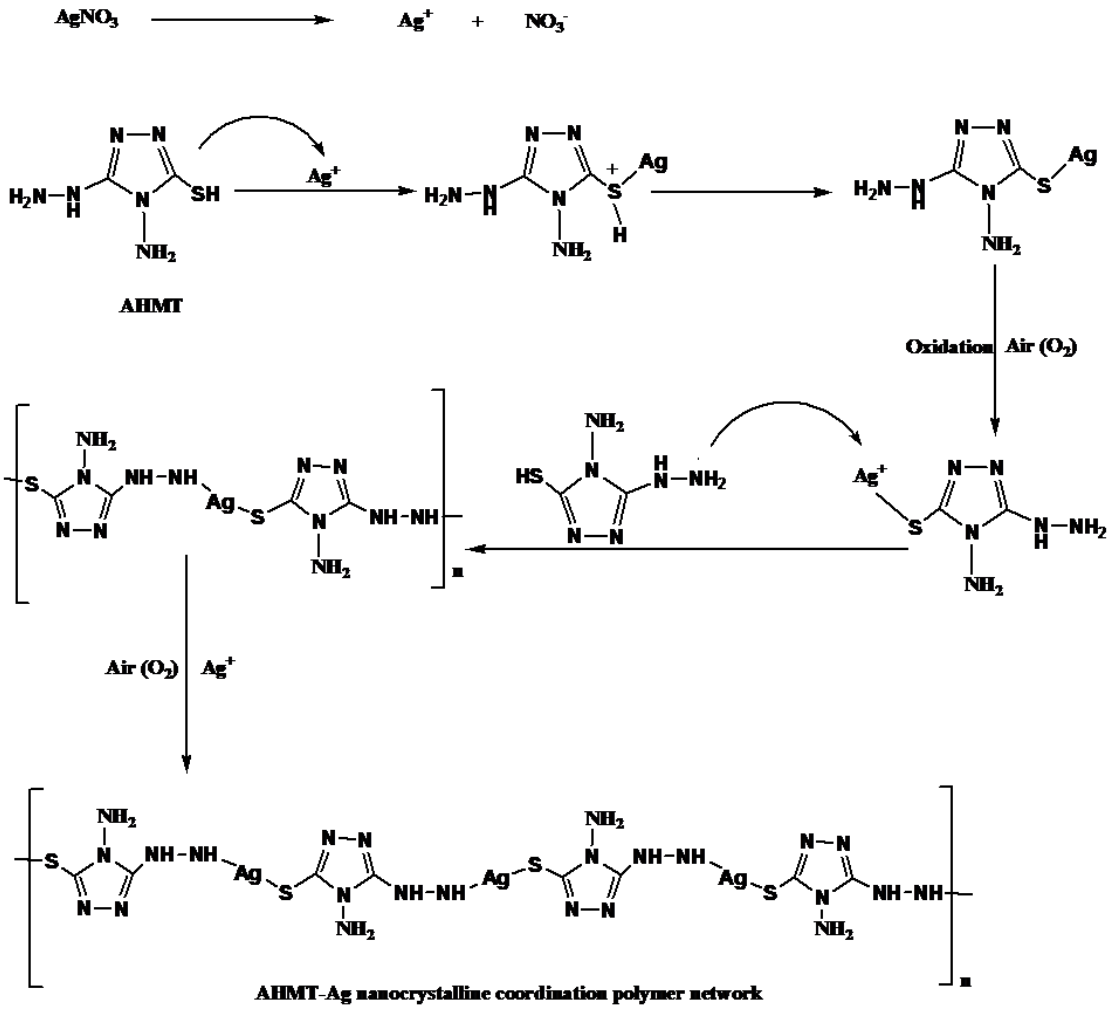

Figure 7.1 Possible mechanism for formation of AHMT-Ag.

At present, there is a number of life saving drugs frequently used in everyday, when their amount exceeds above certain level causes toxicity. 6-meracaptopurine (6-MP), an excessively important immunosuppressive drug, is used as anticancer chemotherapy for dealing acute lymphoblastic leukaemia and inflammatory bowel disease. Generally, the 6-MP concentration was found to be unpredictably highly and low variable in plasma, with manifest individual differences. Hence, it is very essential to monitor the concentration of 6-MP over time.

Numerous approaches have been devoted for detection of 6-MP in biological preparation and pharmaceutical comprising capillary electrophoresis [Yang et al., 2016], high-performance liquid chromatography [Abdelsayed et al., 2017], laser-induced fluorescence [Waterval et al., 2000], spectrofluorimetry [Shahrokhian et al., 2012], chemiluminescence [Fan et al., 2010]. However, these methods require tedious experimentation. Electrochemical approaches have shown notable advantages in the investigation of drugs in human urine and pharmaceutical preparations. These methods in pharmaceutical analysis are studied owing to their accuracy and precision, low cost, simplicity and rapidity, sensitivity.

In this research work, voltammetric method have been applied to depict the electrochemical nature of 6-MP on the carbon paste electrode in the presence of highly electro-active AHMT-Ag NCCP as a suitable nano-sensor in phosphate buffer (pH 7). Further, the developed sensor was effectively explored to assay 6-mercaptopurine in real samples blood serum, urine and tablet.

7.2 Experimental section

7.2.1 Chemicals and materials

AHMT was purchased from sigma Aldrich USA. Silver salt ($AgNO_3$), 6-mercaptopurine monohydrate (6-MP), TEMPO, sodium hydroxide and BHT were bought from SRL chemical (India) and used as accepted unless mentioned otherwise. Aqua regia was used for cleaning of the glassware, after rinse with mixture of ultrapure water and ethanol, Merck India. 6-mercaptopurine solution was freshly equipped by using doubly deionized water and ethanol mixture solution (1:1). The electrodes used to prepare carbon-paste electrode were procured from Bio–analytical Organization. Human urine and blood serum samples were obtained from authorized hospital. The tablet of 6-mercaptopurine was acquired through local supplier (Cipla Ltd. India)

Reaction solutions were exposed in the pure nitrogen to remove oxygen and avoid any external oxidation during each electrochemical measurement.

7.2.2 Electrode fabrication

1 mm diameter Carbon paste electrode (CPE) used for modification was obtained from BASi (Indiana). Carbon paste was prepared by mixing 67% w/w graphite powder, 2.5% w/w paraffin oil and 35% w/w AHMT–Ag then the cavity of electrode was filled with the portion of resulting paste. The surface of CPE was smoothed against butter paper and rinsed with the distilled water. The carbon paste was cautiously removed prior to the pressing a new fraction into electrode after each measurement.

7.2.3 Instrumentation

The Perkin- Elmer 783 spectrometer was used to record FT-IR spectra of AHMT-Ag and AHMT in range of 3600 to 500 cm^{-1} on the KBr disc. Powder X-Ray Diffraction were executed in the range of 5° to 80° by using Miniflex 600 diffractometer with Cu–Kα radiation (Kα =1.54056 Å) with 2°/min scan rate. UV-Vis was performed in quartz cuvette (1cm path length) by the Biotech, Epoch 2 microplate reader spectrophotometer, USA. For elemental analysis XPS (X-ray photoelectron spectrometer) was executed with, Shimadzu Group Company, Kratos analytical instrument, XPS (UK), with 1.254 Å Mg Kα radiations. Nova, Nano-SEM 450 FEI (Netherlands) was used for the record HR-SEM. FEI TECHNAI G^2 20 TWIN Czech Republic electron microscope was used for record HR-TEM, EDS mapping and EDX (Energy Dispersive X-ray) with 200 keV (accelerating voltage) on copper grid (carbon-coated) prepared by 6 µL of polymer solution. Mettler Toledo TGA/DSC 1 STARE System, Switzerland was used for the thermal analysis. TGA and DTA were performed in the inert atmosphere with heating rate 10 °C min^{-1}. All electrochemical measurements were accomplished on Ω Metrohm,

797 VA, Computrace analyzer, Switzerland, using three electrode assembly by electrochemical software 3.1 with AHMT-Ag modified Carbon Paste Electrode (working electrode), Pt foil (counter electrode), Ag/AgCl (reference electrode) and pH 7.0 phosphate buffer used as supporting electrolytes for all electrochemical measurements.

7.2.4 Experimental procedure for AHMT-Ag Synthesis

13.5 mM aqueous/ethanolic solution of AHMT and 100 mM ethanolic solution of $AgNO_3$ were prepared. Further, the $AgNO_3$ solution was dropwise added in AHMT solution with continuous stirring for 24 h at atmospheric pressure and room temperature. Blackish-grey precipitate of the AHMT-Ag nanocrystalline coordination polymer was obtained then obtained precipitate was three times washed after filtration followed by water-ethanol mixture solution to remove the unreacted AHMT and $AgNO_3$. Removal of solvent was regulated at 40 °C in vacuum and the obtained yield was 87%. (Figure 7.2)

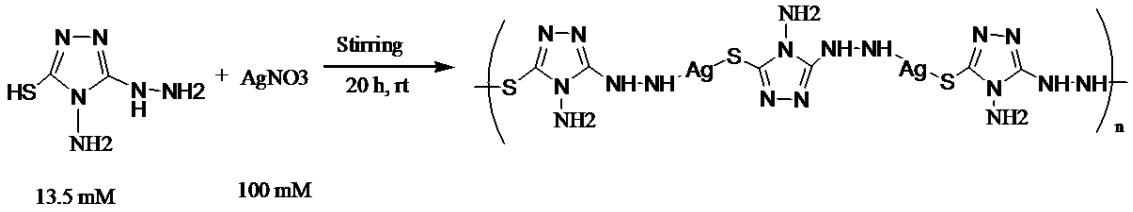

Figure 7.2 Reaction scheme for synthesis of nanocrystalline coordination polymer AHMT-Ag.

7.3 Results and discussion

Coordination polymer AHMT-Ag is a remarkably symmetrical architecture which provide coordination position for the bonding and construct well–predictable network with various interactions and unique capacity to frame π stacking all over aromatic array. Here, sulphur and nitrogen atoms of AHMT coordinated with Ag (I) into a huge

array of polymeric chain. The synthesized AHMT-Ag was characterized by UV-visible, XPS, FT-IR, XRD, ^{1}H NMR, HR-TEM, HR-SEM, EDS mapping, EDX and thermal study.

The radical controlled experiments with BHT (2,6–di–t–butyl–4–hydroxytoluene) and TEMPO (2,2,6,6–tetramethyl–1–piperidinyloxidanyl) trapping agents, endows the cationic pathway without any interference under standard conditions (Figure 7.3). Mechanism involves silver ions as a cationic companion for initiating the polymerization and launching silver associated monomeric segment, which activate Ag oxidation to furnish AHMT-Ag. [Shi et al., 2012] (Figure 7.1). Thereafter structural and bonding information is reviewed under FT-IR, ^{1}H NMR and XPS analysis.

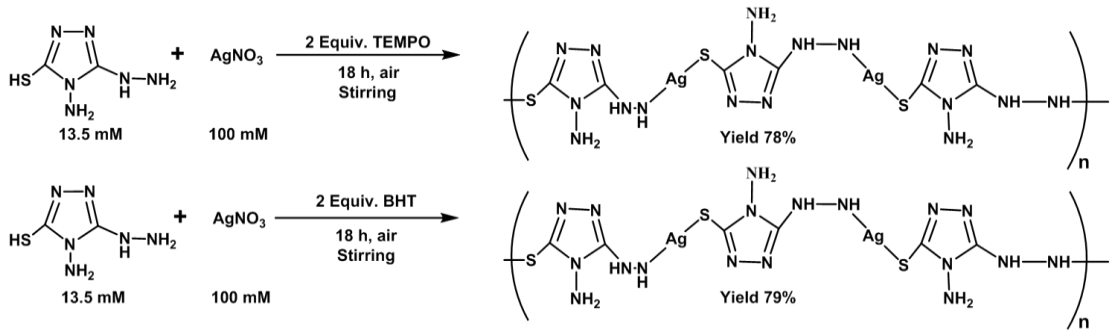

Figure 7.3 Schematic illustrations of controlled experiments for the formation of AHMT-Ag using TEMPO and BHT.

7.3.1 Materials characterizations

The FT-IR spectrum of AHMT shows various bands in the region 3270-2930 due to υ (N-H) and υ (NH_2). The peak broadness recommends intramolecular hydrogen bonding. (Figure 7.4 I). The vibrational band at 3209 cm^{-1} is initiated due to υ ($NH-NH_2$) of AHMT and remarkably attenuated to 3095 cm^{-1} in AHMT-Ag, spotting the connection of the exocyclic $NH-NH_2$ with Ag. Additional, the S–H stretching of AHMT evidenced at 2789 cm^{-1}get disappeared in AHMT-Ag; which indicate thiol ionization, bonding of sulphur *via* silver atom. The thioamide band I at 1501 cm^{-1} in AHMT appeared at higher

wave number 1633 cm^{-1} in AHMT-Ag caused by a decrease in major contributor υ(N–H), and a substantial increase in minor contributor υ(C=N) respectively; due to sulphur and silver bonding. Furthermore, typical thioamide band II 1315–1346 cm^{-1} in AHMT with significant contributor υ(C=N) increased considerably to 1365 cm^{-1} in AHMT-Ag, therefore encourages bonding of silver with sulphur.

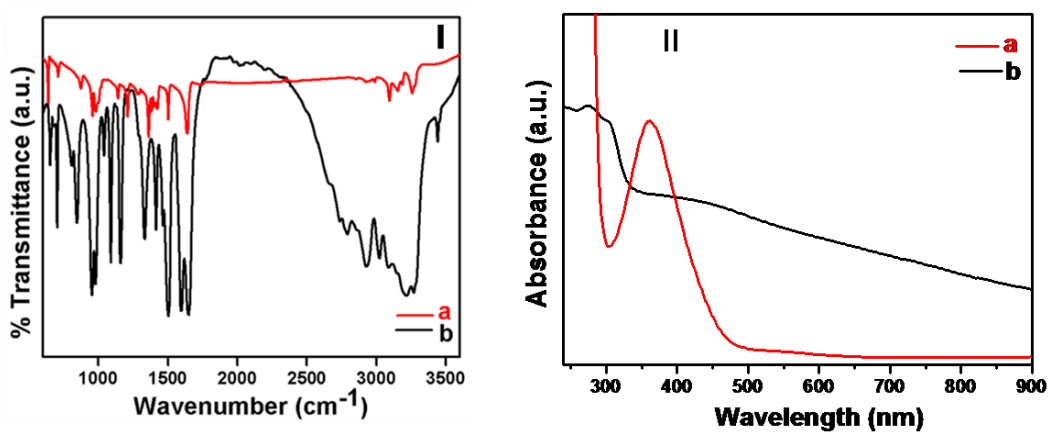

Figure 7.4 (I) FT-IR of spectra (a) AHMT-Ag (b) AHMT and (II) Absorption spectra of (a) AHMT and (b) AHMT-Ag.

Further X- ray diffraction was executed in order to investigate crystal structure. The X-ray diffraction of AHMT-Ag and AHMT were correlated with Ag (0) attained from JCPDS file (CAS number 87-0720). AHMT-Ag displays crystalline nature as shown in Figure 7.5 I. It is noticeable that structural characteristics of AHMT and Ag (0) are absent in AHMT-Ag. The crystallographic phase of AHMT-Ag, NCCP was examined at room temperature by X-ray diffraction (XRD) with a diffraction angle between 5º and 80º. The, DICVOL04.51 (auto-indexing program) was employed to index the XRD pattern of AHMT-Ag [Rodríguez et al., 1993]. It was found that experimental diffraction peaks could be indexed using monoclinic, orthorhombic and triclinic cells. In order to determine the correct crystallographic symmetry for the observed XRD spectra of AHMT-Ag was investigated by Le-Bail refinement through FullProf [Boultif et al.,

1991] for different probable crystal structures; e.g. orthorhombic Pnma, monoclinic $P2_1/m$, Pm and triclinic P1 space groups. It shows that the triclinic crystal structure has the closest fit between calculated and experimentally observed profiles of AHMT-Ag with a good Figure of merit, and it indexed all the diffraction peaks. The Figure 7.5 (II) reveals the experimentally observed data point are indicated with dotted red circles, while the calculated pattern is shown as a continuous solid line and the variation of observed from calculated pattern is shown by continuous bottom green line obtained by Le-Bail fit for space group "triclinic P1". The vertical lines indicate the Bragg peak locations in the difference plot. From Figure 7.5 II, it can be clearly observe that the diffraction peaks emerge in the pattern representing good crystalline nature of synthesized AHMT-Ag NCCP. Triclinic cell has the lattice parameters a = 11.055(1), b = 4.4964(1), c = 5.6471 (2), α= 91.62(4) β= 93.34(1) γ=90.28(2) and unit cell volume 280.30(1) A^3.The crystallinity of AHMT-Ag is again examined by selected area diffraction of TEM. The diffraction peaks of AHMT-Ag are indexed.

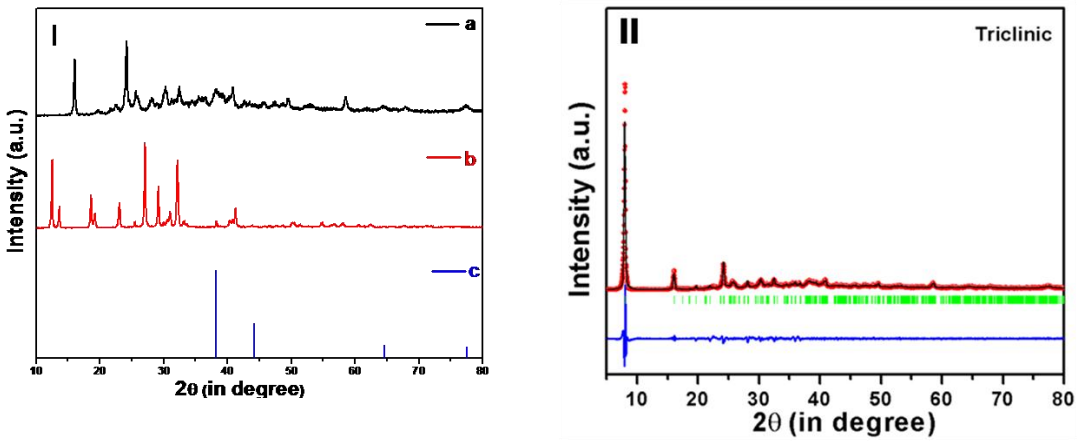

Figure 7.5 (I) X-ray Diffraction of (a) AHMT-Ag (b) AHMT and (c) Ag (0) obtained from JCPDS (CAS no. 87-0720.) file. (II) Le-bail fit of AHMT-Ag.

The absorption spectra difference shows the interaction effect of metal (Figure 7.4 II). AHMT has remarkable absorbance at 360 nm, and the fellow AHMT-Ag reveal

characteristic absorbance 270 nm. Signature of hypsochromic shift in absorbance spectra is due to the interaction between AHMT and Ag. X-ray photoelectron spectroscopy (XPS) enlightens the chemical environment of the elements in AHMT-Ag and oxidation state of the Ag center. The fitted peaks using software, XPS peak 4.1 (Figure 7.6) imparts two doublets fitted for the Ag (3d). The specific peak at 376.2 eV is centered feature peak of the $3d_{3/2}$ Ag(I) [Wang et al., 2013], meanwhile peak at 370.4 eV is the signature of the $3d_{5/2}$ Ag (I) support oxidation state of the silver. N (1s) peaks deliver 5 sets of the singlet in which peak at 403.7 eV is correspond to the binding energy of endocyclic amine nitrogen (=N–). Binding energy of 402.7 eV attributed to –NH groups, superior binding energy acquainted to the bonding of silver with nitrogen of –NH. Additionally binding energy at 400.6, 402.1 and 401.4 eV corresponds to nitrogen of $–NH_2$, C-N-C and C-NH- [Daems et al., 2014; Lee et al., 2016]. The binding energy at 164.6 eV appears due to sulphur (2p3/2). A variation of binding energy favors coordination of the Silver atom with exocyclic sulphur. Binding energy at 287.8 eV and 286.8 eV denotes C(1s) spectrum the for the suitable fit analogous to N=C–N– and —N=C–S– bonding [Lv et al., 2014].

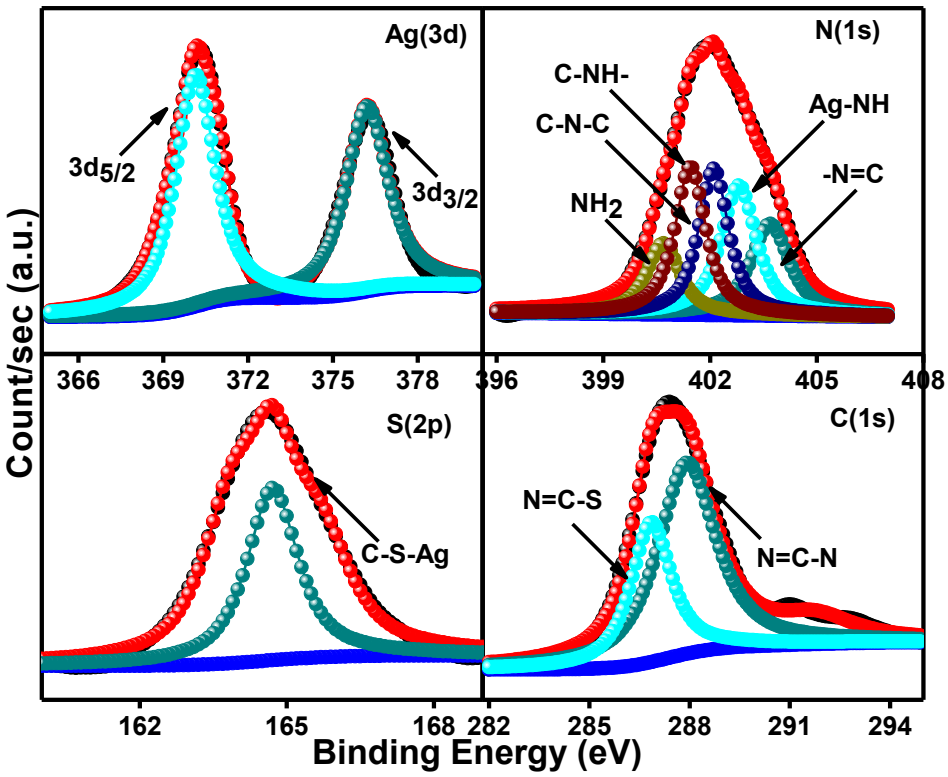

Figure 7.6 XPS spectra of the AHMT–Ag for Ag (3d), N (1s), S (2p) and C (1s) regions.

^{1}H NMR Spectrum of the AHMT has signals at 12.8 signifies for the ring NH, 7.13 for NH of the $NHNH_2$, 5.4 for SH and 5.264 ppm for NH_2 of the $NHNH_2$ protons relative to the TMS. The absence of signal due to the SH proton in AHMT-Ag NCCP establish the bonding of silver through sulphur. Peak appeared at 4.10 ppm is due to the NH_2 of NNH_2 in AHMT-Ag. The peak of $NHNH_2$ and NH observed at lower field i.e. 5.265 and 7.135 ppm respectively in AHMT-Ag furnishes bonding of silver with $NHNH_2$ group of AHMT. The signal corresponding to S=C-NH proton at 8.406 diminishes in AHMT-Ag NCCP which may be due to bonding of metal with sulfur atom of C-S. The doublet at 5.438 also vanished in AHMT-Ag assigning intraction of metal with NH_2 group of NH-NH_2. The signal corresponding to N-NH_2 remained in AHMT-Ag emphasize the unreacted proton of amino group (Figure 7.7).

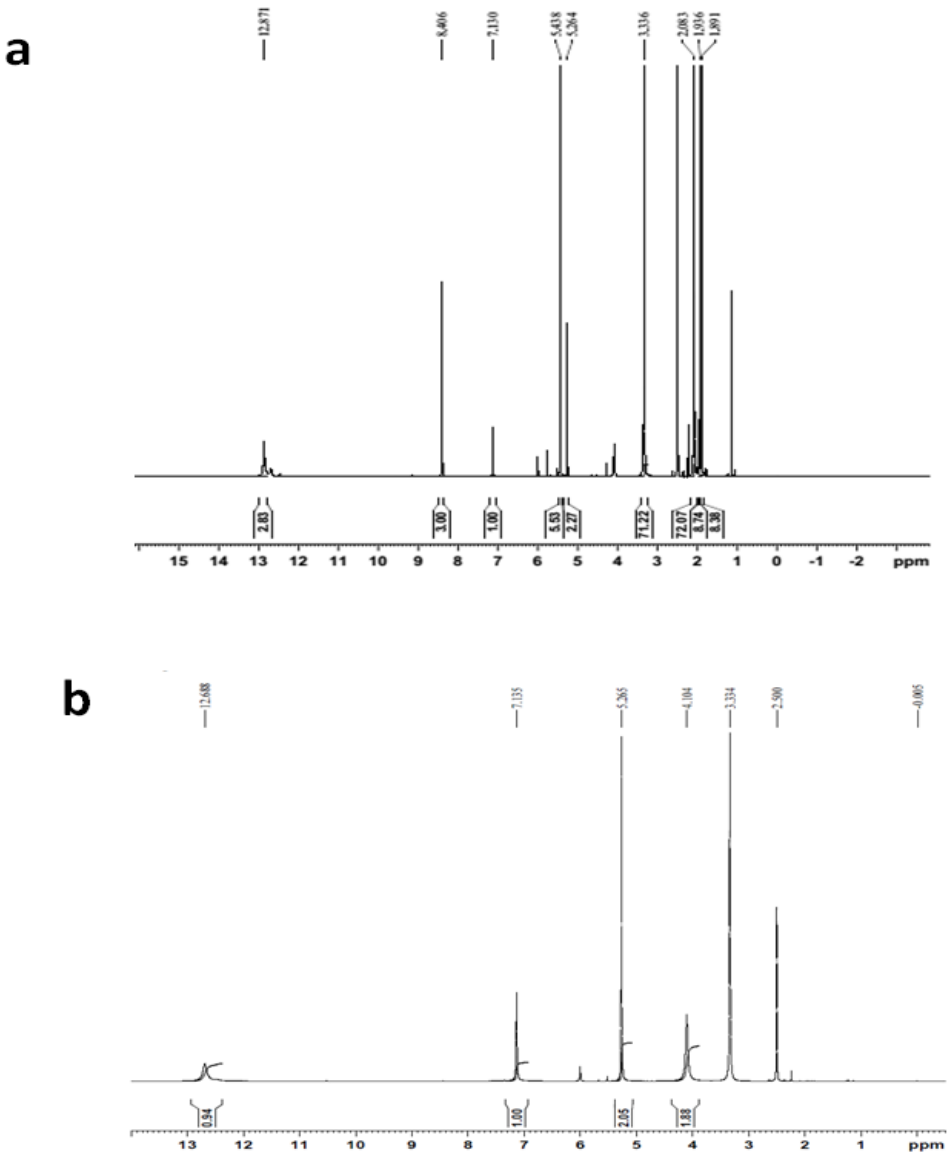

Figure 7.7 ^{1}H NMR of (a) AHMT and (b) AHMT -Ag.

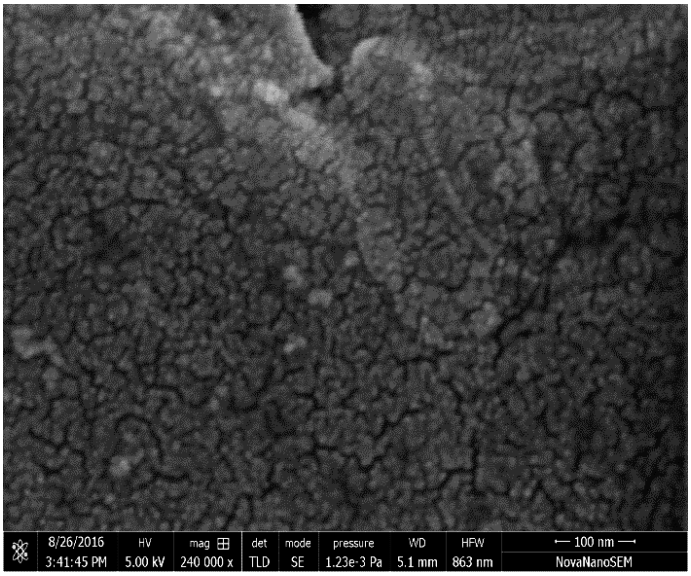

Figure 7.8 HR SEM of AHMT-Ag.

The morphology and elemental investigation of AHMT-Ag, explored by HR-TEM, HR-SEM and SAED pattern shown in Figure 7.8, 7.9 provoke crystalline nano globular shaped network structure (Figure 7.8). The average particle size distribution of AHMT-Ag NCCP was analyzed with Image J software and it shows average size 20-30 nm (Figure 7.9c). The irregular nano globules profile of the distinct AHMT-Ag was also captured in HR-TEM micrograph Figure 7.9a and 7.9b. The SAED pattern illustrates the crystalline nature of AHMT-Ag network (Figure 7.9d). The corresponding EDX measurements reveals the elemental composition of the AHMT-Ag verifies the presence of S ,N , C and Ag atoms in selected area as presented in Figure 7.10. The EDS mapping (Figure 7.11) illustrate elemental composition of AHMT-Ag. Here, the overlap image discloses homogeneous distribution of Ag, C, N and S signifying formation of dense polymeric chain. The consequent images (Figure 7.11) reveals the mapping of discrete elements and evidences the higher nitrogen concentration.

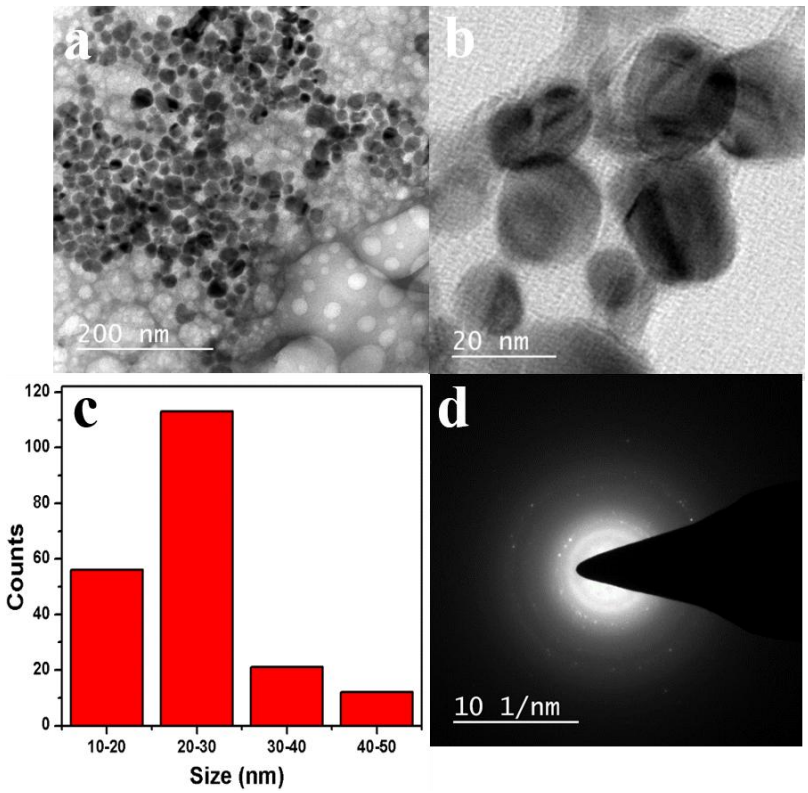

Figure 7.9 HR TEM of AHMT-Ag (a, b), size distribution graph from TEM image (c) and corresponding SAED pattern (d).

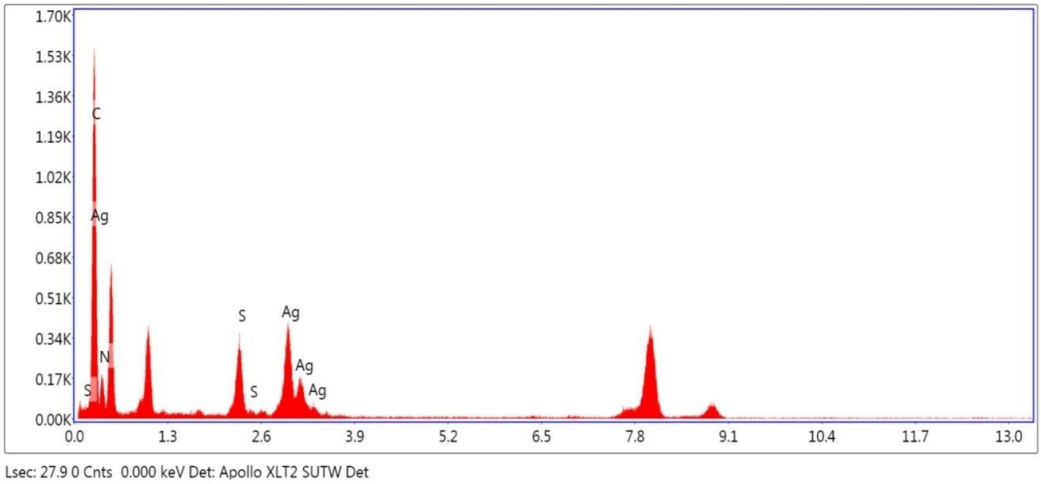

Figure 7.10 EDX of AHMT–Ag provided by HR-TEM graph.

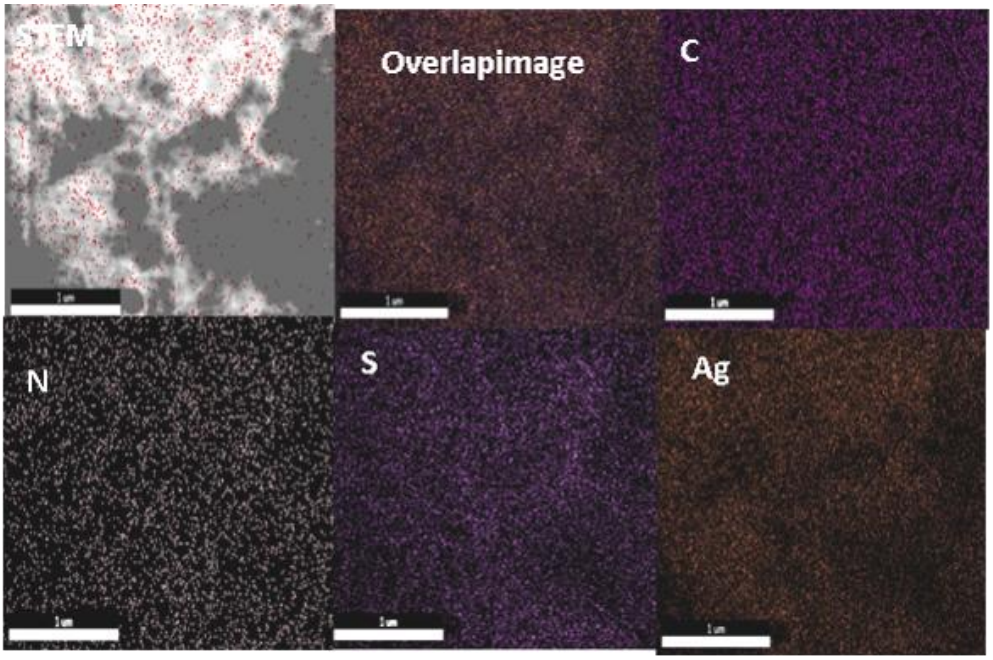

Figure 7.11 EDS Mapping of AHMT-Ag.

For molecular mechanics calculations, the minimum energy state of the two extreme possible organizations of two consecutive units of AHMT-Ag in the polymeric chain was investigated by molecular mechanism dynamics (Figure 7.12). The two possible organizations are assumed to be fused in (1) *syn* and (2) *anti* alignment. The dynamics calculations are tuned to the presence of additional dipole–dipole interaction with the several other interactions parameter by changing the arrangements of the polymeric chain (*cf.* Table 7.1). The resulting comprehensive increase in energy is caused by disturbance of orbital coplanarity [[Ioniţă et al., 2011; Antila et al., 2015]. The table discloses that the total energy is minimum for *anti*–alignment inspite of *syn*–alignment.

Table 7.1 Interaction parameters involved in three AHMT–Ag molecular fusions.

Energy (kcal/mol)	*Syn*–alignment (1)	*Anti*–alignment (2)
Stretch	0.7246	0.5771
Bend	65.5120	15.2109
Stretch–Bend	-0.9156	-0.6244
Torsion	0.1347	0.0801
Non 1,4–VDW	-4.5590	-4.7476
1,4–VDW	3.1204	2.9196
Charge–charge	–	–
Charge–dipole	–	–
Dipole–dipole	-0.5513	1.7324
Total energy	63.4657	15.1481

Where,

Bend energy:	Arises from displacement of bond angle from their equilibrium state.
Stretch energy:	Arises from displacement of bond (contraction or elongation) from their equilibrium state.
Torsion energy:	Arises from steric and electrostatic non bonded interaction of atoms.
VDW= van der Waal force:	Arise from interaction between electron clouds around two non–bonded electrons.
Non VDW:	Arises from electrostatic or non–atom centered charges.
Charge–dipole:	Arises from interaction of charge and dipole.
Charge–charge:	Arises from displacement of electron resulting dipole formation
Dipole–dipole:	Arises from displacement of electron resulting dipole formation.

1

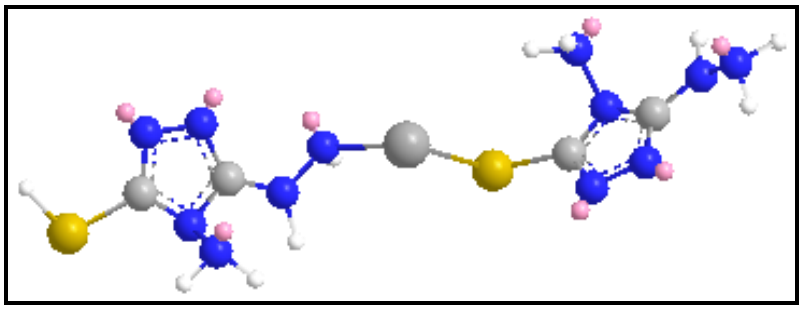

2

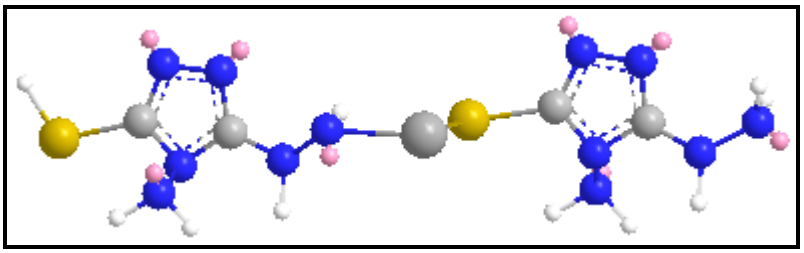

Figure 7.12 Ball-stick model structure of AMT–Ag in the (1) *anti* and (2) *syn* orientation generated by CS 3D Chem bio–draw with structural energy minimization. Here blue, cyan, light grey, golden, dark grey (large size) and pink balls represent N, H, C, S, Ag atoms and lone pairs.

Moreover, the molecular modelling is implemented to achieve the favoured orientation of the ligand in the network, which certifies anti–alignment, the favoured orientation (Figure 7.12). Further, there could be three possible ways for coordination of Ag with ligand 4-amino-3-hydrazino-5-mercapto-1, 2, 4,-triazole (AHMT). Density functional theory (DFT) study was executed in order to assess the most probable way of interaction. Two ligand units were under investigation with metal. Geometries of all the dimers were optimized in water solvent using the B3LYP [Lee et al., 1988] functional and LanL2DZ basis set for Ag atom and 6-31g** basis set for rest of the atoms. The genuineness of the calculated structures was confirmed by visually examining the Vibrational modes related to all real vibration frequencies. All the calculations were accomplished by Gaussian [Frisch et al., 2009] program and Gauss View program was used for visualization of optimized structures and Vibrational modes. A most

appropriate structure has been proposed after the coordination of Ag with AHMT. Three possible structural considerations were optimized using DFT (Figure 7.13). Gibbs free energies of all the three structures of Ag-coordinated AHMT dimer were obtained at the B3LYP/6-31G**+LanL2DZ level of theory in water solvent. N-Ag-S structure was more stable than N-Ag-N and S-Ag-S by 1.44 eV, 4.62 eV and 4.43 eV respectively.

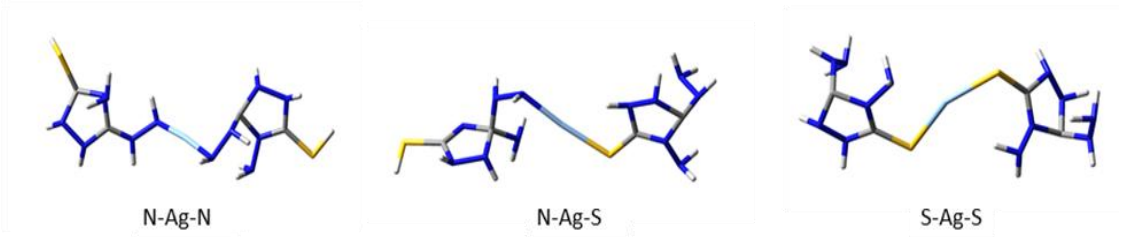

Figure 7.13 Three possible structures of the AHMT dimer coordinated with Ag atom obtained at the B3LYP/6-31G**+LanL2DZ level of theory in water solvent.

Based on the findings the structure of nanocrystalline AHMT-Ag is proposed (Figure 7.14). Ag (I) centers linked with coordination sites of AHMT via sulphur and nitrogen atoms throughout the arrangement and adjacent layers are stabilized through π stacking of the aromatic ring and the intermolecular hydrogen bonding.

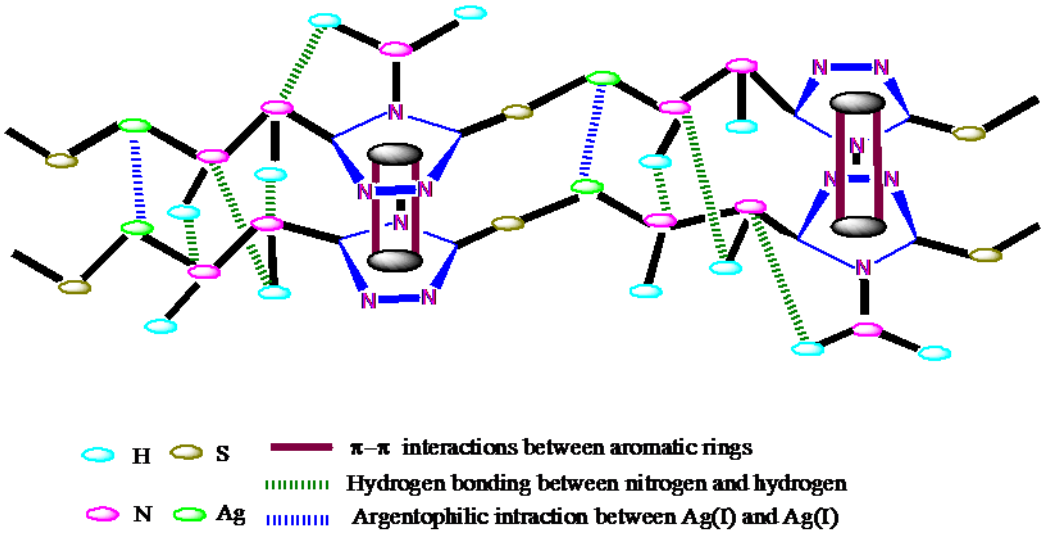

Figure 7.14 Proposed Structural network of AHMT-Ag.

Zeta potential of prepared nanocrystalline coordination polymer was measured by using the Dynamic light scattering (DLS) instrument. The charge on the NCCP plays a important role in accumulation. Larger positive or negative charge repels each other and prevents accumulation. Zeta potential at -49 mV shows the extensively stable network of NCCP (Figure 7.15) [Meléndrez et al., 2010].

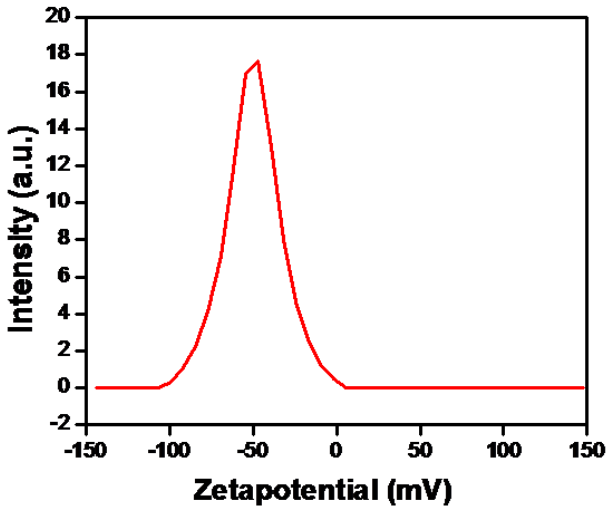

Figure 7.15 Zeta potential of AHMT-Ag.

Thermo–gravimetric properties of AHMT-Ag are studied under a nitrogen environment for analysis of the thermal stability and thermal decomposition activation energy. The thermal decomposition of the AHMT-Ag was illustrated by thermal–gravimetric curve TGA (Figure 7.16). It shows a significant weight loss revealing thermally stabile until 222°C disclosing thermally strong network of coordination polymer. Here, first decomposition at 222°C corresponds to the rupture of the coordination linkage. The minor degradation detected at the 100°C is due to uncoordinated water molecules further, consecutive degradation in TGA plot is due to thermal breakdown of byproducts [Kaya et al., 2014]. Activation energy of the AHMT-Ag related to thermal

degradation is determined *via* Broido equation [Broido et al., 1969]] as 11.39 kJ/mol (Figure 7.17).

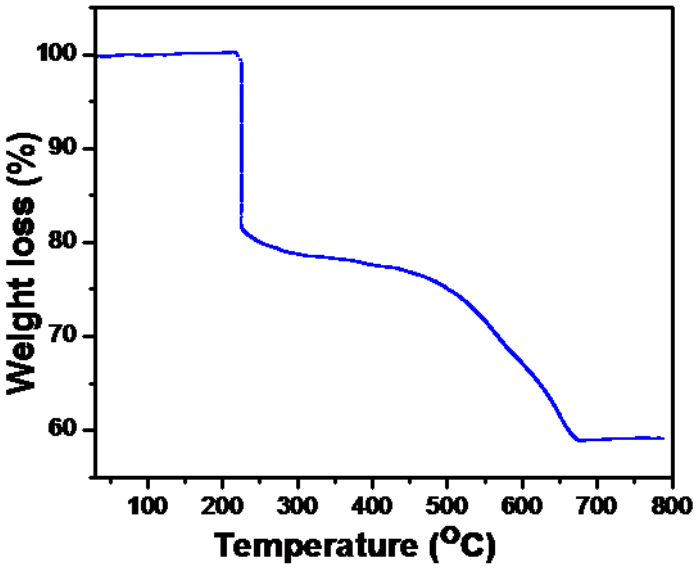

Figure 7.16 TGA plot of AHMT-Ag.

Broido has illustrated a method for the activation energy estimation related to thermal degradation. The equation for the determination of activation energy (E_a) is

$$ln\,[ln(1/Y)] = -(E_a/R)\,1/T + constant \qquad \text{Eq.7.1}$$

Where $Y = W_t - W_\infty / W_0 - W_\infty$

Y is a fraction of a number of beginning molecules still not degraded; weight at time t is W_t, weight at an infinite time is W_∞ (= zero) and initial weight is W_o. A graph of $ln[ln(1/Y)]$ *vs.* $1/T$ yields a good estimation to a straight line (Figure 7.17).

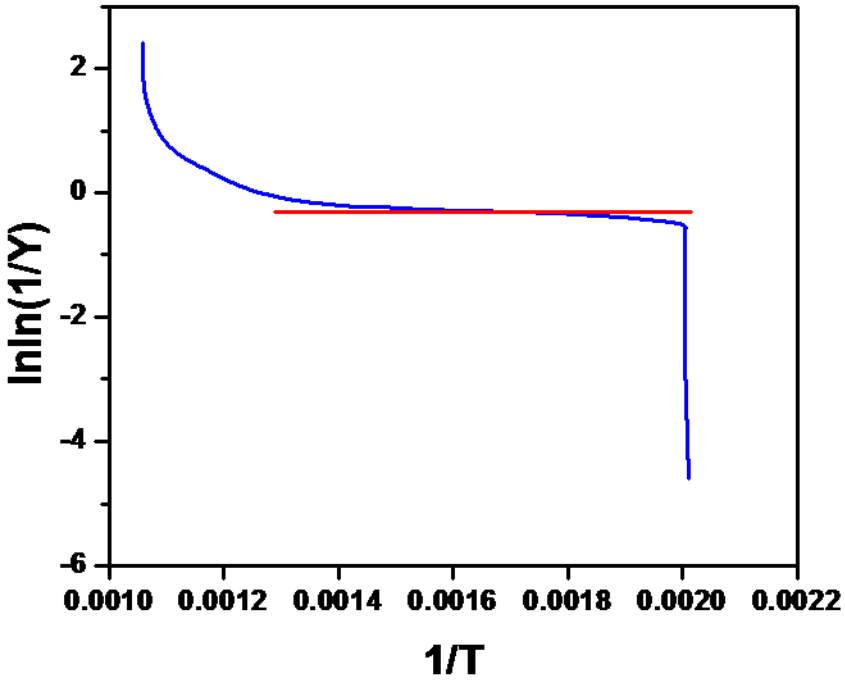

Figure 7.17 Thermal activation energy plot of AHMT-Ag.

The slope of plot $(^{E_a}/_{R})$ corresponds the activation energy for thermal decomposition of AHMT-Ag as 11.39 kJ/mol.

7.3.2 Electro activity of AHMT-Ag

7.3.2.1 Electrode Active surface area

Electro activity of AHMT–Ag NCCP modified carbon paste electrode surface is probed by Fe(III)/Fe(II) redox system and unmodified CPE, AHMT–Ag/CPE active surface area are calculated as 0.03 cm^2 and 0.14 cm^2. These reveal substantial rise in AHMT-Ag/CPE effective surface area by factor of 4 caused by larger exposure and density in the nano-architecture modified electrode (Figure 7.18).

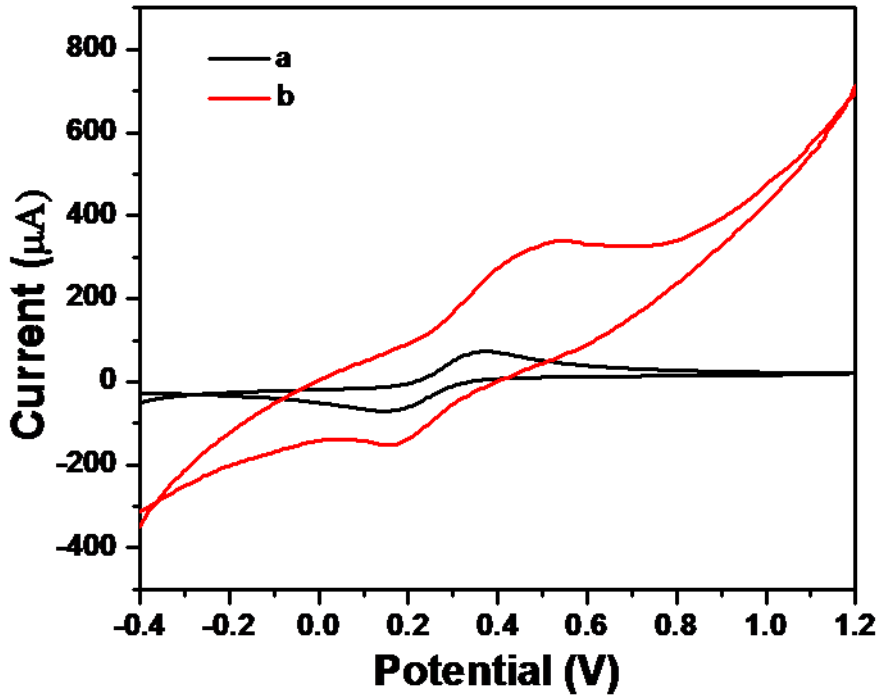

Figure 7.18 The CV of the electrodes in 5 mM Fe (III) in PBS pH 7 unmodified CPE (a) and AHMT-Ag modified CPE (b).

7.3.2.1.1 Calculation of active surface area the electrode

Electro activity of AHMT-Ag NCCP modified carbon paste electrode surface is probed by Fe(III) /Fe(II) redox system and unmodified CPE, AMT-Ag/CPE active surface area are calculated using Randles–Sevcik equation (Eq.7.2).

$$i_p = 2.69 \times 10^5 n^{3/2} A D^{3/2} C \upsilon^{1/2} \qquad \text{Eq.7.2}$$

Here C is concentration of Fe(III), n present the electron involved in electro–oxidation, D shows diffusion coefficient of the Fe(III) /Fe(II) redox system, and A stands for the effective surface area of unmodified CPE and AHMT-Ag/CPE, calculated as 0.03 cm^2 and 0.14 cm^2. These evaluations reveal substantial rise in AHMT-Ag/CPE effective surface area by factor of 4 caused by larger exposure and density in the nano-architecture modified electrode (Figure 7.18).

7.3.2.2 Number of electrons transferred (n_a)

The electrons involved in the electro-oxidation of 6-MP (n_a) is calculated as 1.64 using Laviron equation (Figure 7.20a, c) and ensure irreversible oxidation of 6-MP is two electron procedure at AHMT-Ag/CPE, followed by previous report [Keyvanfard et al., 2013].

7.3.2.2.1 Estimation of the number of electrons transferred (n_a)

A plot of i_p (anodic current) *vs* $\upsilon^{1/2}$(square root of the scan rate) is sketched (Figure 7.20 b) which ensure nature of the electro-oxidation; mechanism on AHMT-Ag/CPE follows adsorption or diffusion controlled path. Linearity of graph at R^2 0.997 recommend that 6-MP oxidation at AHMT-Ag/CPE followed by the linear equation (Eq.7.3) is diffusion controlled process.

$$i_p = (2.99 \pm 0.05)\upsilon^{1/2} - (2.50 \pm 0.32) \qquad \text{Eq.7.3}$$

Further, the ordinate non–zero intercept, describes adsorption on the surface of electro-active electrode.

7.3.3 Optimization of Reaction Condition

7.3.3.1 Effect of the pH

Effect of the pH on electrochemical detection of 6-MP was studied, and the results are shown in Figure 7.18 The AHMT-Ag modified carbon paste electrode shows maximum anodic current for 6-MP oxidation at pH 7 which suggests that 6-MP oxidation is much more sensitive to pH 7. Thus, the pH of buffer was optimized 7 for the whole quantification spectrum of drug.

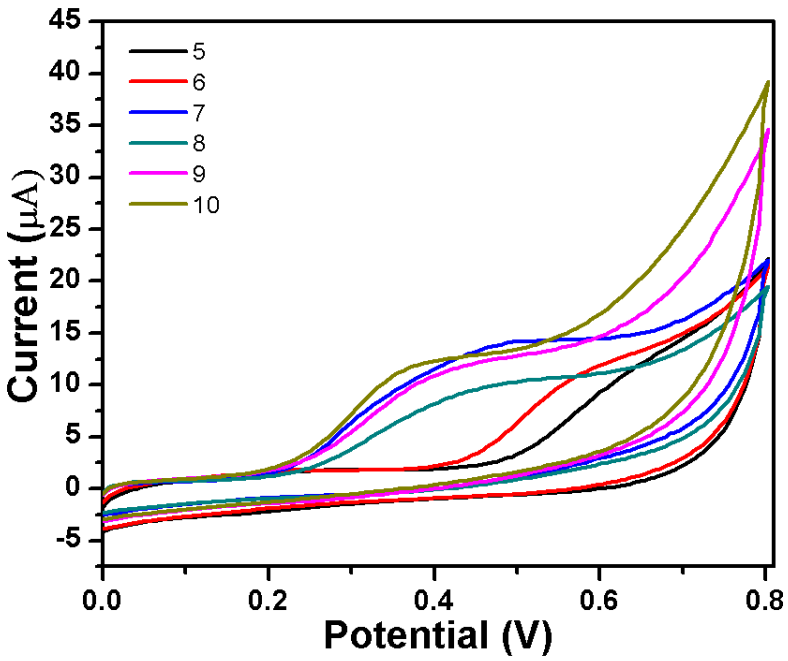

Figure 7.19 Cyclic voltammetric (CV) response by the serial addition of 6-MP to AHMT-Ag/CPE in PBS at different pH.

7.3.3.2 Effect of the Scan rate

The plot of i_p (anodic current) *vs* $\upsilon^{1/2}$(square root of the scan rate) displays the diffusion-controlled mechanism of 6-MP electro-oxidation; on AHMT-Ag/CPE and explores adsorption on the surface of electro-active electrode (Figure 7.19 b).

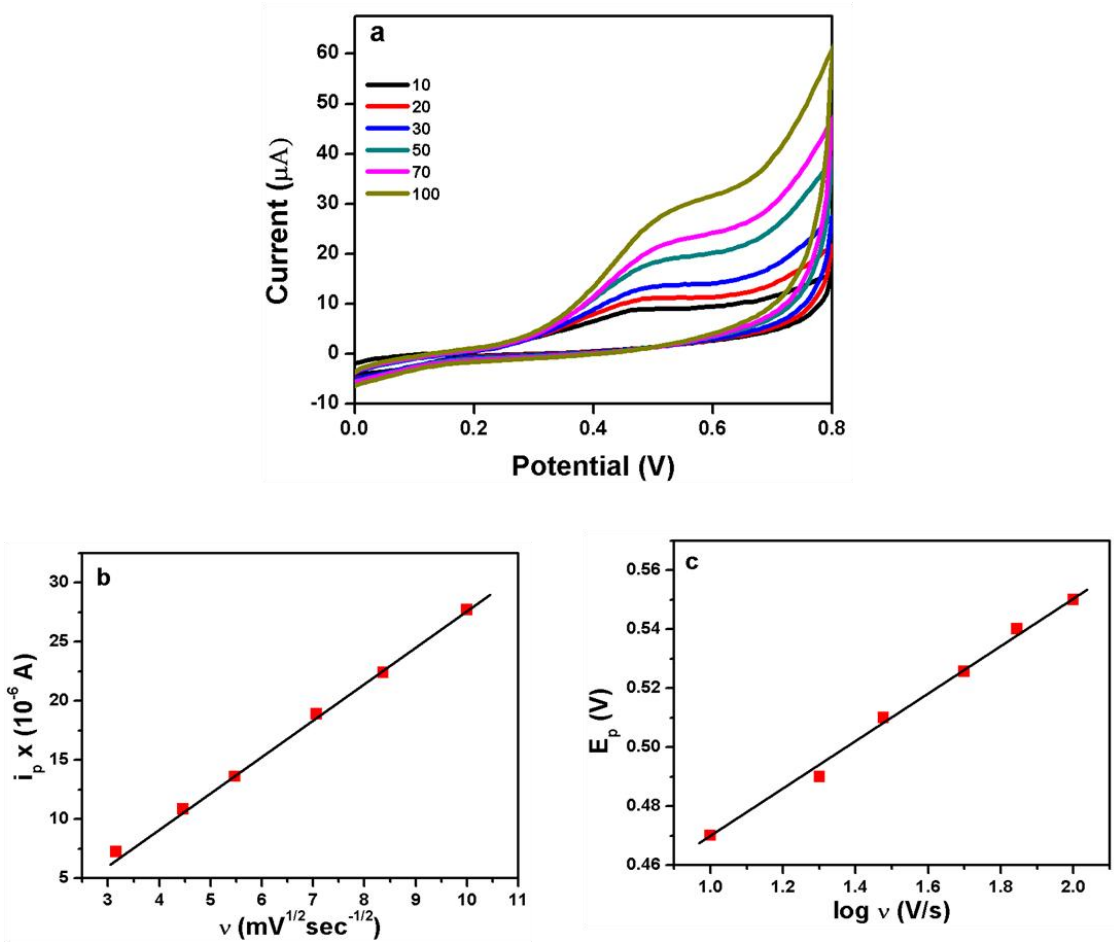

Figure 7.20 (a) CV of AHMT–Ag/CPE in 18 µM 6-MP at scan rates 10, 20, 30, 50, 70 and 100 mV, (b) plots of the 6-MP anodic peak current against $\upsilon^{1/2}$ and (c) anodic peak potentials against log υ.

7.3.3.3 Effect of Matrix

Effect of Matrix is the collective effect of several ingredient of the sample other than the analyte during the quantitative analysis. It reduces or increases the analyte response. Dilution with solvent is the best approach to suppress the matrix effects. Therefore, mixed blank serum and PBS (pH 7.0) were both spiked with 6-MP (60 µM), diluted with PBS (pH 7.0) at 20, 50, 100, 120 and 150-fold, and analyzed, respectively to explore the matrix effect. At 20-fold dilution, the serum discloses lower anodic peak current and higher anodic peak potential than PBS (Figure 7.21A), and (Figure 7.21B). Increasing the dilution, the peak current remains stable and the anodic peak potential

reduces from 50 to 100-fold in serum. Contrary, the peak current diminishes sharply while the peak potential rises slightly in PBS. For 100-fold onwards dilution, anodic peak current and potential have almost constant values. These outcomes demonstrate the 100 times dilution evidences the elimination of matrix effect of serum and guarantees the high sensitivity and thus adopted for the consequent analysis.

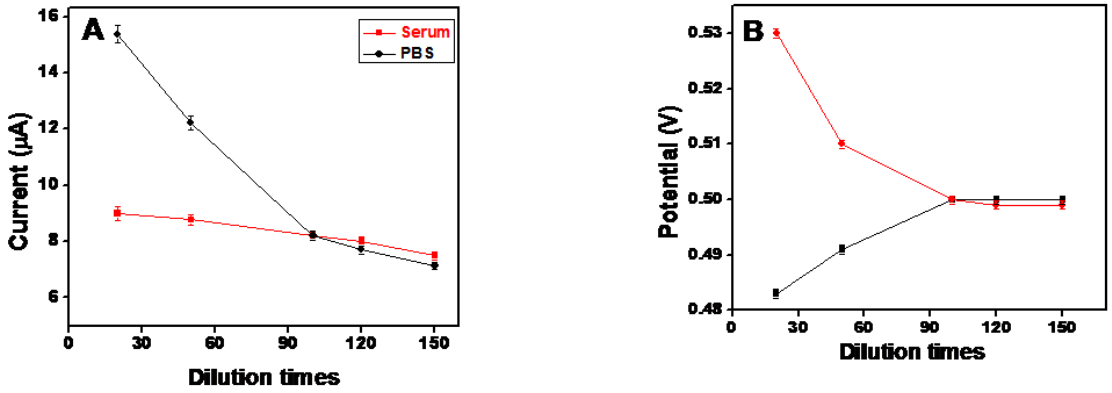

Figure 7.21 Effect of Matrix on the anodic peak current and potential, (A) anodic current vs. dilution times, (B) peak potential vs. dilution times. The spiked concentration of 6-MP in serum is 60 μM (mean ± SD for n = 5).

7.3.4 Electrochemical detection of 6-MP

The electro activity of AHMT-Ag/CPE was explored for the thorough and broad-spectrum voltammetric assay of 6-MP in PBS at optimized pH 7. A featured anodic signature exhibits at 0.48 V in voltammogram of CV and DPV using AHMT-Ag/CPE is a crucial signature of 6-MP electro-oxidation. In order to establish the complete experimentation, plot for the consecutive addition was observed (Figure 7.22) which shows anodic peak enhancement with the successive addition in both CV and DPV. The calibration graph for DPV executes linear dependency of anodic current with drug concentration and provides limit of detection as 21 nM and sensitivity 0.56 μA/ μM with regression value 0.99 at the S/N ratio (signal/noise): 3.

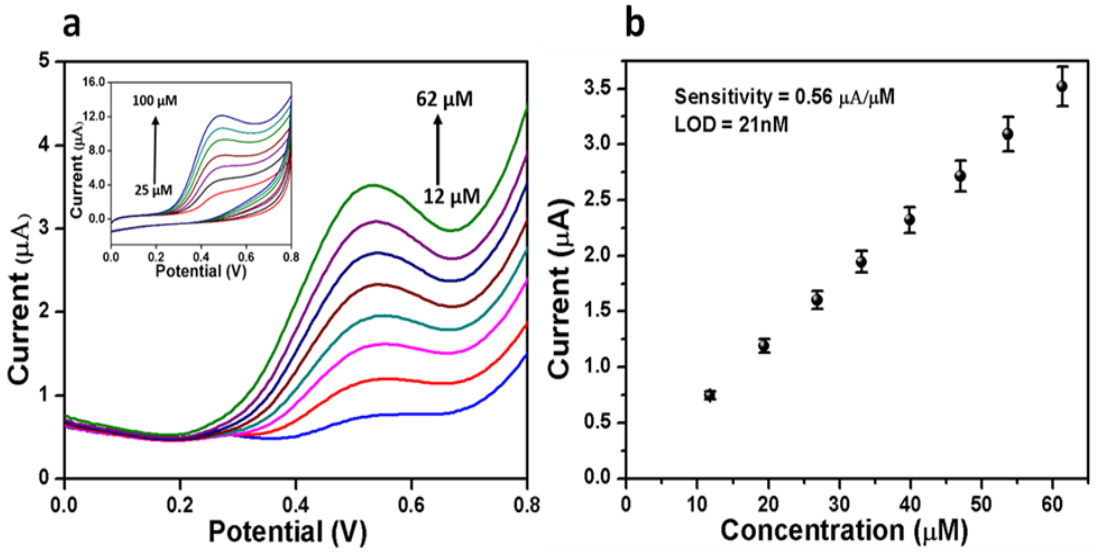

Figure 7.22 (a) Differential pulse voltammogram recorded on AHMT–Ag/CPE in 0.1 M PBS (pH 7) by successive addition of 6-MP, inset of (a) cyclic voltammogram recorded by successive addition of 6-MP, (b) corresponding calibration plot (for DPV).

The anodic peak increases significantly with the sequential addition of drug since the AHMT-Ag modified electrode indorsed the electro-oxidation of 6-MP. Here 6-MP approaches to the modified electrode and get attached. The driving force for the endorsement of attachment and electro-oxidation is (a) intermolecular hydrogen bonding between amino groups, (b) the effective electron channeling of AHMT-Ag which assist the faster electron transfer through electrode, (c) the π-π electron coupling of aromatic rings, (d) hydrophobic interaction between duplex AHMT-Ag and 6-MP, (e) high surface area of AHMT-Ag, (f) electro–catalytic efficiency of Ag promote the electro–oxidation of 6-MP. The schematics for electro-oxidation of 6-MP at AHMT-Ag platform is presented, it occurs through transfer of two electrons and two protons and electron channelling occurs through the AHMT-Ag platform (Figure 7.23).

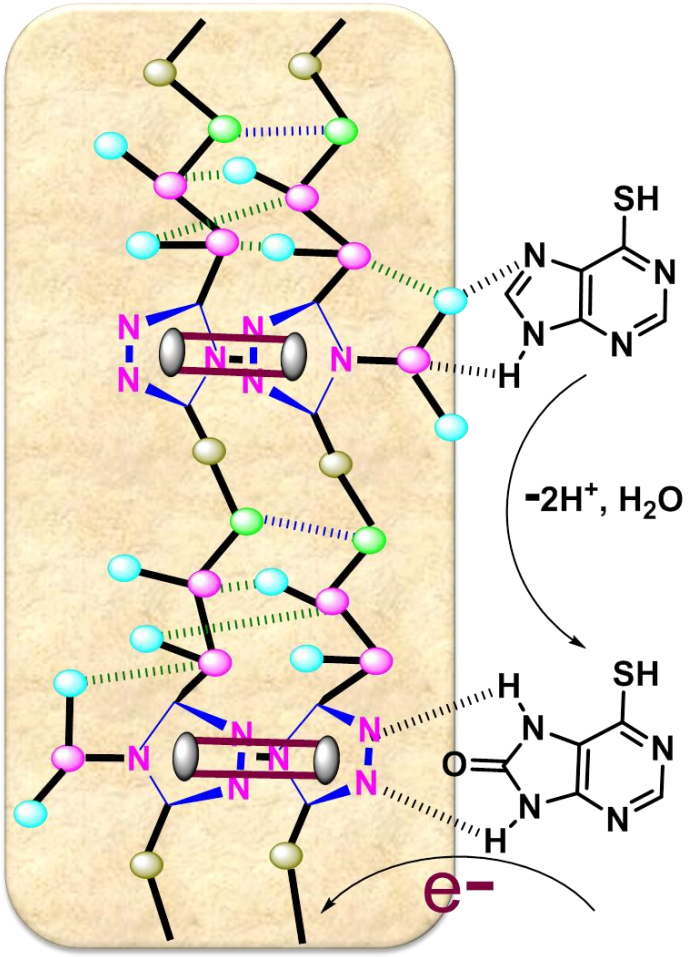

Figure 7.23 Mechanism for electro–oxidation of 6-MP.

In order to verify the broad-spectrum applicability of the sensor, the AHMT-Ag/CPE was used to assay 6-MP in pharmaceutical formulation of drug. The sample solution was developed in buffer and pH was maintained 7. This spiked solution of tablet was utilized for the voltammetric assay in same experimental condition optimized for ideal situation using both CV and DPV and shown in Figure 7.24. The CV and DPV response for the successive addition of drug exhibit anodic peak at 0.48 V with corresponding to 6-MP oxidation. The corresponding calibration plot for the detection shows linear response of anodic current with concentration of 6-MP up to 120 µM with limit of detection 37 nM and regression value 98% validating the sensing approach in clinical formulation.

7.3.5 Validation of Method

Various constituents present in serum and urine coexist therefore the primary objective of this report was to assess and explore the ability of the sensor to assay 6-MP in urine and serum. The urine and serum samples were diluted and buffered to pH 7. The developed sensor explores the dependence of anodic peak current of 6-MP on concentration. The plot for consecutive addition is displayed (Figure 7.25, 7.26) which provides limit of detection 97 nM and 87 nM respectively using DPV results. In the light of these results, the developed sensing platform is highly sensitive and versatile for detection of 6-MP which is authenticated in clinical formulation, human urine as well as serum samples. The characteristic envisioned anodic current event figured at 0.48 V. Further, the proposed method was compared with various reported methods for 6-MP detection through bar diagram (Figure 7.27). The proposed system provides least detection limit among the existing literature for 6-MP assay and thus supports the better efficiency of the designed sensor.

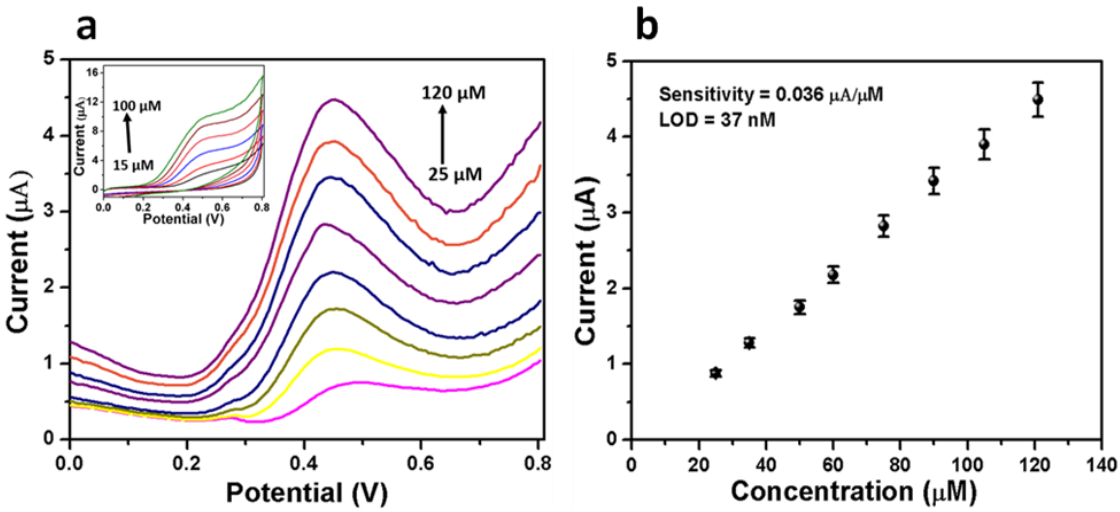

Figure 7.24 (a) Differential pulse voltammogram recorded on AHMT–Ag/CPE in 0.1 M PBS (pH 7) by successive addition of 6-MP Tablet, inset of (a) cyclic voltammogram recorded by successive addition of 6-MP, (b) corresponding calibration plot (for DPV).

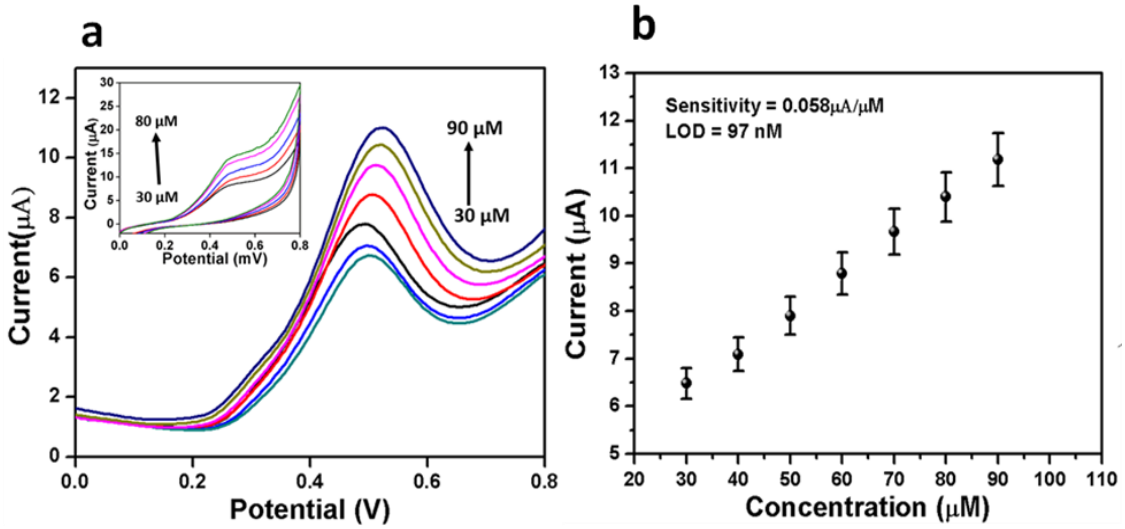

Figure 7.25 (a) Differential pulse voltammogram recorded on AHMT–Ag/CPE in urine sample by successive addition of 6-MP, inset of (a) cyclic voltammogram recorded by successive addition of 6-MP, (b) corresponding calibration plot (for DPV).

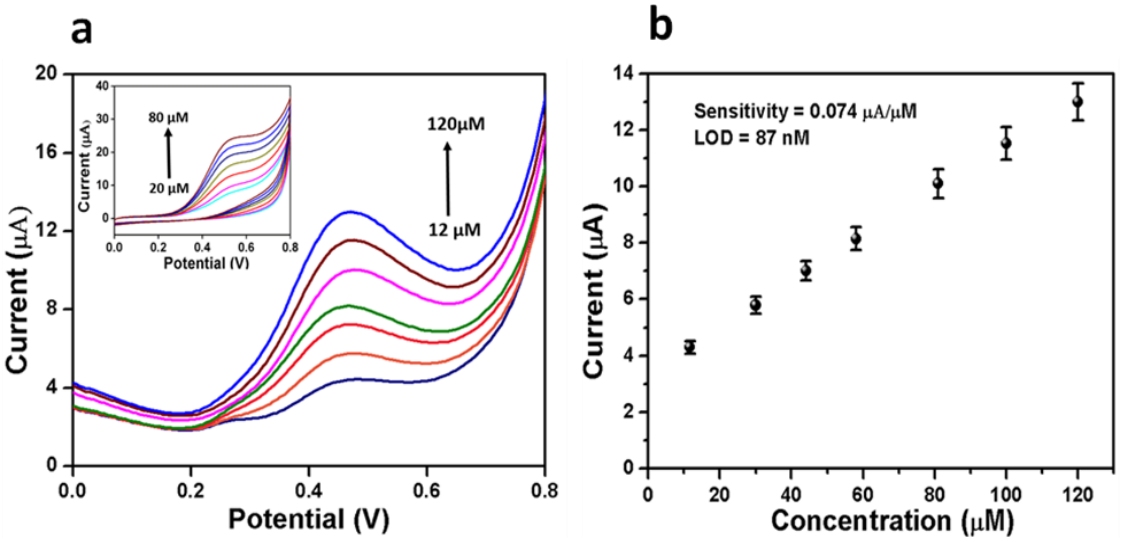

Figure 7.26 (a) Differential pulse voltammogram recorded on AHMT–Ag/CPE in serum sample by successive addition of 6-MP, inset of (a) cyclic voltammogram recorded by successive addition of 6-MP, (b) corresponding calibration plot (for DPV).

Serum sample was investigated by the electrochemical assay. Pearson's correlation analysis discloses a substantial relationship of 6-MP concentrations in serum analyzed by electrochemical method ($r = 0.9131$, $0 < p < 1$) (Figure 7.26)

The matrix effect of serum has been studied with direct dilution and avoided the complex modification process. The sensitivity of the method was significant covering fairly low and lethal 6-MP concentrations. This encouraging work is to develop of a simple, accurate and practical electrochemical method for the determination of 6-MP in plasma for clinical diagnosis.

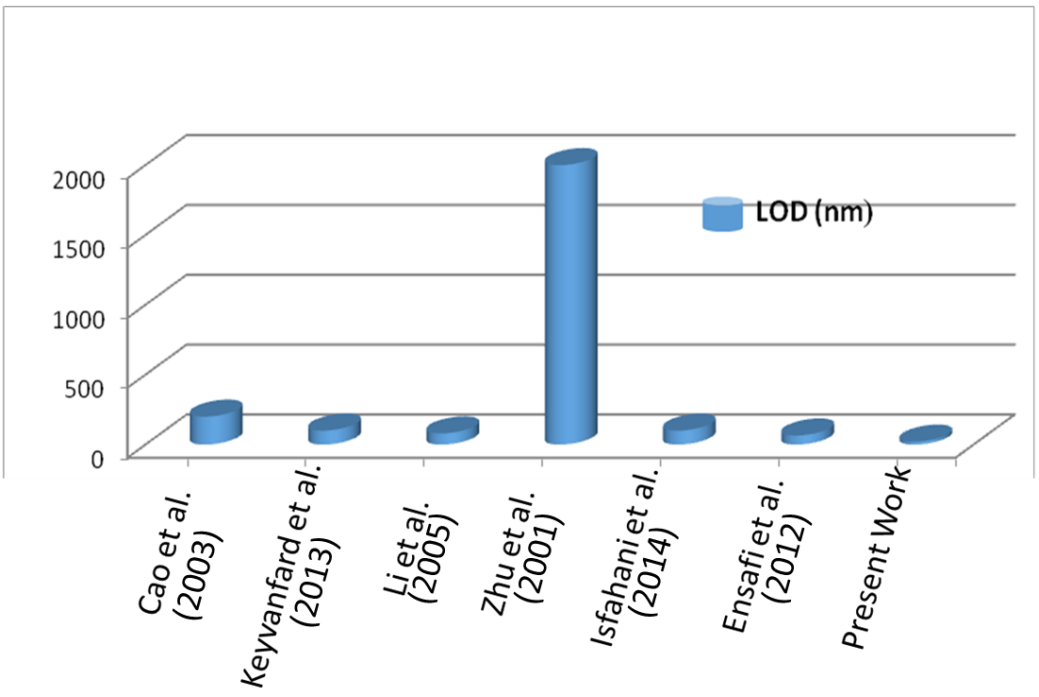

Figure 7.27 Analytical Figure for the comparision of present work with other methods.

7.3.6 Interference study

Interference study was performed to examine the specificity of the electrochemical sensor by using 6-MP (55 µM) with and without 100-µM solution of interfering substances through the designed electrochemical technique (Figure 7.28). It can be noticed that electrochemical current response deviation due to interfering agent was 5% of without interferences, representing excellent selectivity of designed electrochemical.

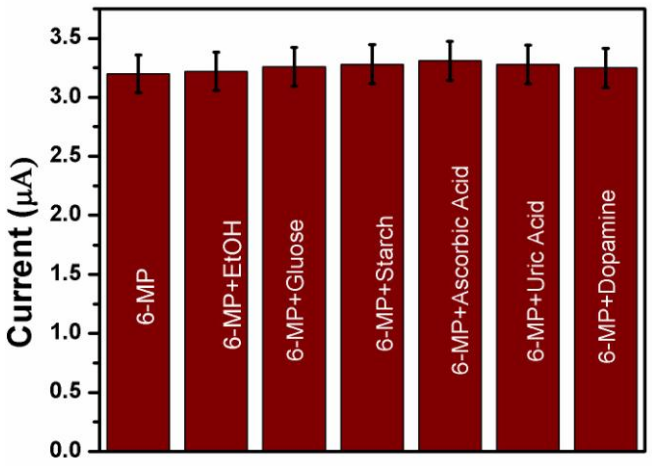

Figure 7.28 Differential pulse Voltammetric (DPV) responses of electrochemical sensor to 55 µM 6-MP, 55 µM 6-MP+ 100 µM ethanol, 55 µM 6-MP + 100 µM glucose, 55 µM 6-MP+ 100 µM starch, 55 µM 6-MP+ 100 µM Ascorbic acid, 55 µM 6-MP+ 100 µM uric acid and 55 µM 6-MP+ 100 µM Dopamine. Error bar = RSD, (n = 5).

7.4 Conclusions

This article provides development of an elegant nanocrystalline polymeric network of AHMT-Ag which provide a geometrically and symmetrically feasible highly sensitive platform for the ultra-trace and whole spectrum systematic and potential quantification of 6-MP. The effective electron channelling through nanocrystalline architecture is essential for facile production of feature centred events. The complete experimentation depicted that serendipitous use of the AHMT-Ag is a crucial for generating distinctive current pattern in characteristic events. This feature endows high confidence assay at ultra-trace level. The key of success of sensing methodology is the feasible and faster electron channelling through the nanocrystalline polymeric platform. The potential of the study is enzyme-less, cost effective and complete spectrum ultra-trace detection of 6-MP. This strategy can be explored in the commercial portable device fabrication for a variety of anticancer drugs.